

Miniaturizing transmon qubits using van der Waals materials

Abhinandan Antony,¹ Martin V. Gustafsson,² Guilhem J. Ribeill,² Matthew Ware,² Anjaly Rajendran,³ Luke C. G. Govia,² Thomas A. Ohki,² Takashi Taniguchi,⁴ Kenji Watanabe,⁵ James Hone,¹ and Kin Chung Fong^{2,*}

¹*Department of Mechanical Engineering, Columbia University, New York, NY 10027, USA*

²*Raytheon BBN Technologies, Quantum Engineering and Computing Group, Cambridge, Massachusetts 02138, USA*

³*Department of Electrical Engineering, Columbia University, New York, NY 10027, USA*

⁴*International Center for Materials Nanoarchitectonics,*

National Institute for Materials Science, 1-1 Namiki, Tsukuba 305-0044, Japan

⁵*Research Center for Functional Materials, National Institute for Materials Science, 1-1 Namiki, Tsukuba 305-0044, Japan*

(Dated: September 14, 2021)

Quantum computers can potentially achieve an exponential speedup versus classical computers on certain computational tasks, as recently demonstrated in systems of superconducting qubits. However, these qubits have large footprints due to their large capacitor electrodes needed to suppress losses by avoiding dielectric materials. This tactic hinders scaling by increasing parasitic coupling among circuit components, degrading individual qubit addressability, and limiting the spatial density of qubits. Here, we take advantage of the unique properties of the van der Waals (vdW) materials to reduce the qubit area by a factor of > 1000 while preserving the required capacitance without increasing substantial loss. Our qubits combine conventional aluminum-based Josephson junctions with parallel-plate capacitors composed of crystalline layers of superconducting niobium diselenide (NbSe_2) and insulating hexagonal-boron nitride (hBN). We measure a vdW transmon T_1 relaxation time of $1.06 \mu\text{s}$, which demonstrates a path to achieve high-qubit-density quantum processors with long coherence times, and illustrates the broad utility of layered heterostructures in low-loss, high-coherence quantum devices.

Superconducting qubits form an attractive platform to build scalable quantum computers, as recently demonstrated in quantum processors consisting of large arrays of qubits [1]. Achieving fault-tolerant quantum computation would provide a transformative technology in quantum simulation, chemistry, and optimization [2, 3]. However, the industry-standard transmon qubit consists of Josephson junctions (JJ) shunted by capacitors with a large footprint $\sim 10^5 \mu\text{m}^2$. In order to acquire a sufficient capacitance, these capacitors are made of large planar electrodes without dielectric materials that can host two-level systems (TLSs), which are a major source of decoherence [4]. While brute-force scaling using conventional transmons remains possible [5], there is growing interest in alternative approaches that could lay the foundation of next-generation quantum processors. Approaches such as protected qubits can decouple from environmental noise [6], but improving the constituent materials can dramatically impact qubit technology by reducing the footprint and enhancing qubit coherence. As such, new material platforms for qubits are now actively explored [7–13].

Van der Waals (vdW) heterostructures are a promising material platform for quantum devices. Cleaved from pure bulk crystals, the surfaces of these heterostructures are pristine and atomically flat. They can be assembled into stacks with their layers held together by weak bonds without straining the crystals [14]. This architecture allows for diverse properties of various vdW materials, such as gate-tunability [15, 16], high kinetic inductance [17], and giant thermal response to microwave photons [18, 19], which can be exploited for potential quantum applications [20]. Here, we take advantage of

the high-quality vdW heterostructures to fabricate compact vdW parallel-plate capacitors (PPC) using superconducting niobium diselenide (NbSe_2) and insulating hexagonal boron nitride (hBN). We observe quantum coherence of a transmon qubit that uses a vdW PPC as the shunt capacitor. Our result goes against the current trend of requiring large-footprint shunt capacitors in transmons [5], and demonstrates the potential of using crystalline materials to improve qubit coherence.

Fig. 1A shows schematically the fabrication process of the vdW PPC [13] (details in Method). It is different from the conventional process for making high-quality vdW heterostructures [14] because qubits operate in the single-photon regime, where any dissipation or loss channel introduced by the materials or fabrication process can destroy quantum information. Therefore, we assemble each heterostructure within an inert atmosphere to avoid oxidation and contamination of the interfaces. Then, the vdW heterostructure is placed onto the qubit substrate with pre-patterned niobium resonators. To make a vdW transmon, we connect the vdW PPC in parallel with two $\text{Al}-\text{AlO}_x-\text{Al}$ JJs that form a superconducting quantum interference device (SQUID) loop for tuning of the qubit frequency with a magnetic flux generated by a bias current through an off-chip coil. A conventional qubit formed using a planar Nb capacitor and a single JJ is created at the same time for comparison. Fig. 1B schematically shows these elements, with the transmons capacitively coupled to the readout resonator (red) and drive line (green). Fig. 1C and 1D show optical micrographs of the assembled vdW PPC ($109 \mu\text{m}^2$ in area and 35 nm in thickness) and the vdW transmon, respec-

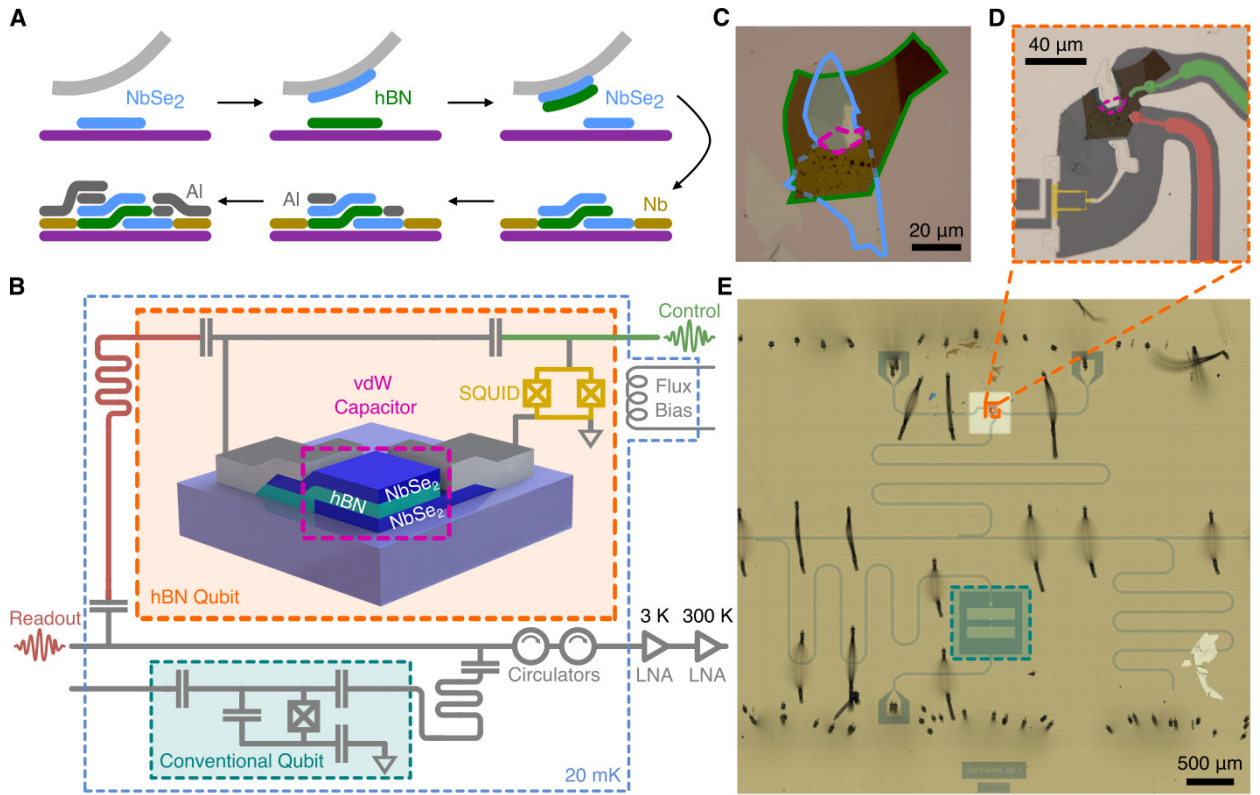


FIG. 1. Fabrication of vdW transmon and measurement schematics. (A) Fabrication procedures for the vdW parallel-plate capacitor (PPC). In clockwise direction: dry polymer-based stacking of vdW heterostructure by sequential pick-up of NbSe₂, hBN, and NbSe₂ flakes. Transfer of the heterostructure to a void within the pre-patterned Nb layer on a silicon substrate, deposition of Al contacts, and deposition of JJs and interconnects. (B) Schematic circuit diagram showing our frequency-tunable qubit (orange box) and fixed-frequency conventional qubit (teal box) as a control. Both qubits are coupled to coplanar-waveguide resonators for readout through a common bus line with low noise amplifiers (LNA) after circulators. (C) Optical micrograph of the NbSe₂-hBN-NbSe₂ heterostructure used to make the PPC (pink dashed line) with an area of 109 μm^2 and hBN thickness of 35 nm. (D) Optical micrograph of the vdW transmon formed by the SQUID loop (yellow) shunted by the vdW capacitor with capacitive coupling to the readout resonator (red) and control line (green). (E) Optical micrograph of both qubits in the same field of view, illustrating the miniaturization of transmon qubit by the vdW capacitor.

tively. The optical image in Fig. 1E shows the dramatic size reduction enabled by the vdW PPC, which is about 1400 times smaller than the conventional planar shunt capacitor. For this study, we fabricated and measured two vdW transmons. We fully characterize one of them and present the data in the main text.

We perform spectroscopy experiments to characterize the coupling of the vdW qubit to its readout cavity. With high probing powers, the cavity is unperturbed by the qubit and resonates at 6.9073 GHz with a linewidth of 290 kHz (Fig. 2A). Measuring under low powers, we find the strong coupling with the qubit dispersively shifts the cavity frequency by 1.00 MHz [21]. Fig. 2B shows how the flux-bias current modulates the cavity frequency. We perform qubit spectroscopy by applying a control signal at various frequencies to the qubit while probing the cavity nearly on resonance. Fig. 2C shows the transition frequency, $\omega_{01}/2\pi$, between the ground, $|0\rangle$, and excited, $|1\rangle$, states of the qubit at 5.2815 GHz. Using

the two-photon transition frequency between the $|0\rangle$ and $|2\rangle$ states, i.e. $\omega_{02}/2\pi = 5.216$ GHz, we find the qubit anharmonicity, $\alpha/2\pi, = -131$ MHz. α agrees with the charging energy of the qubit, E_C ($-\alpha = E_C/h$ for a transmon with h being the Planck constant), calculated using the PPC formula with an hBN dielectric constant of 4.4. Fig. 2D shows $\omega_{01}/2\pi$ versus flux-bias current. It has a maximum at ≈ 0.2 mA, which is consistent with the flux dependence of the readout resonator in Fig. 2A and represents the sweet spot where the transmon is the least susceptible to flux noise. In 5 μA steps of flux-bias current, we observe no anticrossing in the qubit spectroscopy due to the coupling of the vdW transmon with coherent TLSs. From the dispersive shift and detuning from the readout cavity, Δ , of 1.6258 GHz at the sweet spot, we find the qubit-resonator coupling, $g/2\pi, = 40.3$ MHz. The Josephson energy, E_J/h , calculated from ω_{01} , is 28.0 GHz. Our qubit is in the transmon regime with $E_J/E_C \simeq 214$.

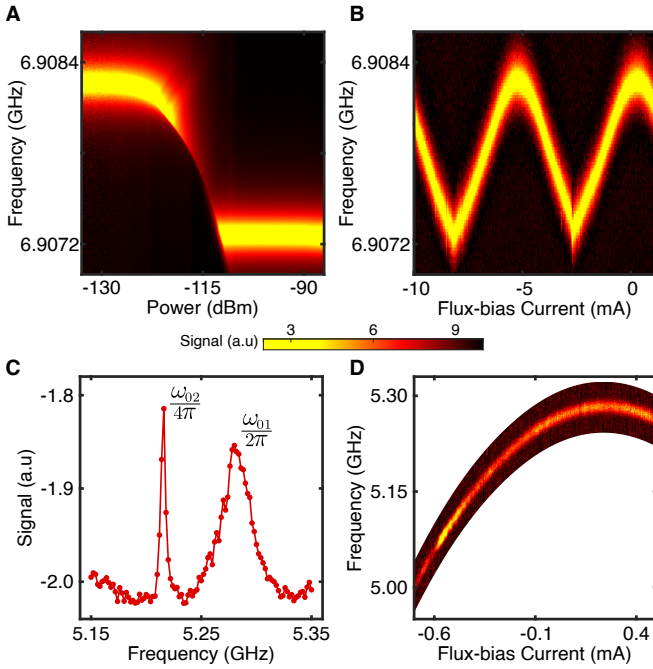


FIG. 2. **Spectroscopy of a vdW transmon** **(A)** Readout-cavity resonance as a function of applied microwave power at the sweet spot of flux bias. **(B)** Readout-cavity resonance versus flux-bias current. **(C)** High power spectroscopy shows the ω_{01} and two-photon $\omega_{02}/2$ qubit transitions at the sweet spot of flux bias. **(D)** Qubit frequency, $\omega_{01}/2\pi$, as a function of flux tuning.

We demonstrate the quantum coherence of the vdW transmon by performing Rabi experiments (see Fig. 3A). By driving the qubit with a resonant pulse for a time, t_{Rabi} , the vdW transmon Rabi oscillates coherently on the Bloch sphere between the ground, $|0\rangle$, and excited, $|1\rangle$, states before being measured using the dispersive shift of the resonator [21]. The oscillation frequency, $\omega_{Rabi}/2\pi$ is set by the drive strength, Ω , and drive detuning from the qubit frequency, $\delta\omega_d$, as $\omega_{Rabi} = \sqrt{\Omega^2 + \delta\omega_d^2}$. When performed at different excitation frequencies and a high pulse power, we obtain the data as shown in Fig. 3B. We quantify the qubit lifetime by measuring the T_1 energy relaxation time at the sweet spot (Fig. 3C). After applying an 80-ns-long π -pulse to excite the qubit from $|0\rangle$ to $|1\rangle$ and waiting for a time delay, t_{delay} , the qubit state is read out. We repeatedly measure the exponential decay of excited state probability, $P_{|1\rangle}$, to quantify the mean and fluctuations of T_1 over a period of 8 hours. The histogram (see inset) shows T_1 of $1.06\ \mu\text{s} \pm 0.09\ \mu\text{s}$ (standard deviation). Next, we quantify the qubit coherence by measuring the dephasing time T_2^* during a Ramsey experiment. Fig. 3D shows the qubit readout signal after the Ramsey pulse sequence of $\pi/2-t_{delay}-\pi/2$. The oscillation is due to $\delta\omega_d$. We fit the data to a decay oscillation and obtain T_2^* of $1.67 \pm 0.20\ \mu\text{s}$. Fig. 3E shows Ramsey oscillations at different qubit drive frequencies.

Finally, we probe for evidence of excessive low frequency noise that may dephase the vdW transmon using a Hahn echo pulse sequence, which contains an additional π -pulse in the middle of the Ramsey sequence. Fig. 3F shows the qubit readout signal after the Hahn echo sequence. We obtain the echo dephasing time, T_{2E} , of $1.72 \pm 0.27\ \mu\text{s}$, that is nearly energy-relaxation limited, i.e. $T_{2E} \approx 2T_1$.

We can compare the performance of our vdW transmon with the conventional one fabricated on the same substrate. The T_1 and T_2^* of the conventional transmon are $11.5 \pm 0.4\ \mu\text{s}$ and $10.5 \pm 0.6\ \mu\text{s}$, respectively. Since both transmons are subjected to the same fabrication process and measurement setup environment, this result suggests that the JJs are not the limiting factor of the quantum coherence of our vdW transmon. On the other hand, based on finite-element simulations, only 87% of the capacitive energy of our vdW transmon design is confined internally to the PPC. This could result in degraded qubit performance through a finite qubit coupling with residue, external to the PPC, from the vdW stacking process or Al lift-off. If we assume the energy relaxation is entirely caused by the capacitive loss and use the equation, $1/T_1 = \omega_{01} \tan \delta$, we can estimate the upper bound of the loss tangent, $\tan \delta$, of the vdW PPC to be 2.83×10^{-5} . This value is not yet intrinsic to the hBN but approaching to $\tan \delta$ of silicon ($\approx 10^{-6}$) as the dielectric in a PPC [22, 23], but our vdW PPC is much more compact. To extend qubit T_1 relaxation, we will need to improve the fabrication process and further concentrate the electric field within the pristine interior of the vdW PPC.

Recently, experiments have taken a similar direction using the intrinsic JJ PPC to make the merged-element transmon (MET) [12, 24]. While both the MET and vdW transmon accomplish miniaturization, the METs demonstrated so far use amorphous insulators which are known to harbor TLSs. As the vdW heterostructure can also function as a high-quality JJ [8, 25, 26], one can envision a future vdW-MET consisting of a crystalline vdW material as the tunnel barrier. Moreover, the thickness of the vdW insulator is defined by discrete-atomic layers. This highly-uniform, crystalline tunnel barrier can potentially allow for a reduced TLS defect density and precise control of qubit frequencies, that can address the frequency-crowding problem [27]. In the future, we plan to extend our result to further miniaturize quantum processors by reducing footprints of circuit components using, e.g. compact lumped-element resonators.

During the preparation of this manuscript, we became aware of a complementary work [28].

Acknowledgements. We thank L. Ranzani for useful discussions. Most of this work was supported by Army Research Office under Contract Number W911NF-18-C-0044. Development of heterostructure assembly techniques at Columbia was supported by the NSF MRSEC

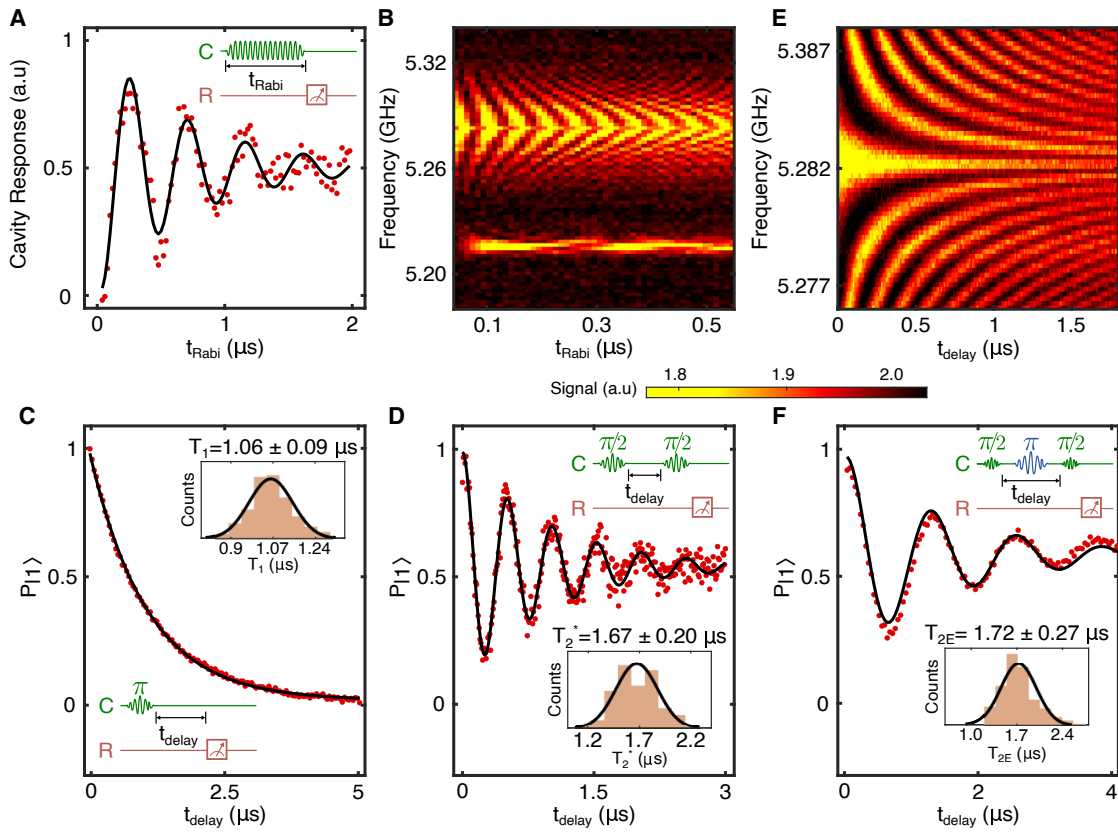


FIG. 3. Quantum coherence of the vdW transmon at the sweet spot of flux bias. (A) Rabi oscillation vs. the pulse width, t_{Rabi} near the qubit frequency. (B) Rabi oscillations at a high power for different excitation frequencies. (C) T_1 energy relaxation time measurement with the pulse control and measurement sequence (inset). The exponential fit yields the T_1 relaxation time. The inset histogram shows data from 8 hours of repeated measurements. (D) Ramsey experiment shows T_2^* dephasing time. (E) Ramsey fringes at different drive tone frequencies. (F) Hahn echo experiment to obtain the echo dephasing time, T_{2E} .

program (DMR-2011736). A.A. thanks the supplemental support from QISE-NET under NSF DMR-1747426. K.W. and T.T. acknowledge support from the Elemental Strategy Initiative conducted by the MEXT, Japan (Grant Number JPMXP0112101001) and JSPS KAKENHI (Grant Numbers JP19H05790 and JP20H00354).

Method Flakes of hexagonal-boron nitride (hBN) and niobium diselenide (NbSe_2) of thickness about 35 and 20 nm, respectively, were exfoliated onto silicon substrates with 285 nm SiO_2 epilayers. The thickness of each hBN flake was measured using atomic force microscopy prior to stacking. Because the NbSe_2 is highly air sensitive, NbSe_2 exfoliation and assembly of the $\text{NbSe}_2/\text{hBN}/\text{NbSe}_2$ heterostructure (Fig. 1A) was performed inside the inert atmosphere of a nitrogen filled glovebox, using a polypropylene carbonate/Polydimethylsiloxane based dry pick-up and transfer process [14]. Since the loss in the polypropylene carbonate is one of the major causes of qubit relaxation, special care was taken to keep the NbSe_2 -hBN- NbSe_2 interfaces clean. The heterostructure was then transferred to a $400 \mu\text{m} \times 400 \mu\text{m}$ sized bare silicon landing site, on a high

resistivity Si substrate coated with 200 nm thick niobium (Nb). Coplanar transmission lines for control and readout resonators, as well as coplanar capacitor pads for a secondary benchmark/control qubit were patterned into the Nb layer prior to the incorporation of vdW materials. E-beam lithography was used to define Ti/Al contacts to the two NbSe_2 flakes. *In situ* ion milling to remove the oxide that forms on the exposed NbSe_2 surfaces prior to deposition was crucial to achieving ultralow-loss contacts [13]. Al-AlO_x-Al JJs were fabricated using standard e-beam lithography and double-angle evaporation. Further steps of e-beam lithography and high quality Al deposition were performed to connect the Nb resonators and ground plane to the contacts and to create superconducting interconnects.

* kc.fong@rtx.com

[1] Arute, F. *et al.* Quantum supremacy using a programmable superconducting processor. *Nature* **574**, 505–510 (2019).

Physical quantity	Value
Readout-cavity frequency, $\omega_c/2\pi$	6.9083 GHz
vdW transmon frequency, $\omega_{01}/2\pi$	5.2815 GHz
Anharmonicity, $\alpha/2\pi$	-131 MHz
Coupling strength, $g/2\pi$	40.3 MHz
Detuning, $\Delta/2\pi$	1.6258 GHz
Josephson energy, E_J/h	28.0 GHz
Charging energy, E_C/h	131 MHz
E_J/E_C	214
JJ normal resistance, R_n	11.2 k Ω
JJ critical current, I_c	11.99 μ A
$E'_J = \Phi_0 I_c/2\pi$	27.4 GHz
PPC area	109 μ m ²
PPC (hBN) thickness	35 nm
PPC capacitance	110 fF

TABLE I. List of vdW parameters. Values from device S111 that is presented in the main text. R_n is measured at room temperature from a JJ fabricated on the same qubit substrate. I_c is inferred from Ambegaokar-Baratoff relation using R_n . E_J is calculated using ω_{01} and α whereas $E'_J = \Phi_0 I_c/2\pi$ is the Josephson energy calculated using I_c with Φ_0 being the magnetic flux quanta. All quantities, if dependent on the flux-bias, are taken at the sweet spot.

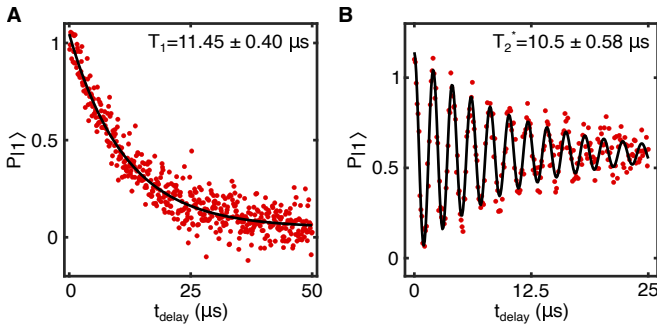


FIG. 4. Quantum coherence of the Conventional transmon. (A) T_1 energy relaxation time measurement. (B) Ramsey experiment shows T_2^* dephasing time.

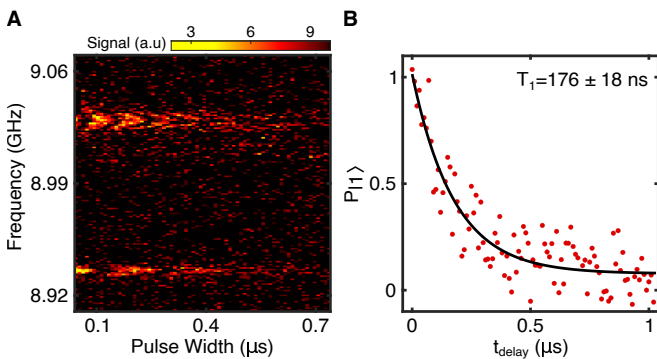


FIG. 5. Quantum coherence of the second vdW transmon device. (A) Rabi oscillations at a high power at different excitation frequencies. (B) T_1 energy relaxation time measurement.

- [2] Cao, Y. *et al.* Quantum Chemistry in the Age of Quantum Computing. *Chem. Rev.* **119**, 10856 (2019).
- [3] Berry, D. W., Childs, A. M., Su, Y., Wang, X. & Wiebe, N. Time-dependent Hamiltonian simulation with L^1 -norm scaling. *Quantum* **4**, 254 (2020).
- [4] Müller, C., Cole, J. H. & Lisenfeld, J. Towards understanding two-level-systems in amorphous solids: insights from quantum circuits. *Rep. Prog. Phys.* **82**, 124501 (2019).
- [5] Gambetta, J. M. *et al.* Investigating Surface Loss Effects in Superconducting Transmon Qubits. *IEEE Trans. Appl. Supercond.* **27**, 1–5 (2017).
- [6] Gyenis, A. *et al.* Experimental Realization of a Protected Superconducting Circuit Derived from the 0– π Qubit. *PRX Quantum* **2**, 010339 (2021).
- [7] Casparis, L. *et al.* Superconducting gatemon qubit based on a proximitized two-dimensional electron gas. *Nat. Nanotechnol.* **13**, 915–919 (2018).
- [8] Lee, K.-H. *et al.* Two-Dimensional Material Tunnel Barrier for Josephson Junctions and Superconducting Qubits. *Nano Lett.* **19**, 8287 (2019).
- [9] Wisbey, D. S. *et al.* Dielectric Loss of Boron-Based Dielectrics on Niobium Resonators. *J. Low Temp. Phys.* **195**, 474–486 (2019).
- [10] McRae, C. R. H. *et al.* Cryogenic microwave loss in epitaxial Al/GaAs/Al trilayers for superconducting circuits. *J. Appl. Phys.* **129**, 025109 (2021).
- [11] Place, A. P. M. *et al.* New material platform for superconducting transmon qubits with coherence times exceeding 0.3 milliseconds. *Nat. Comm.* **12**, 1–6 (2021).
- [12] Mamin, H. J. *et al.* Merged-Element Transmons: Design and Qubit Performance. *Phys. Rev. Appl.* **16**, 024023 (2021).
- [13] Antony, A. *et al.* Making high-quality quantum microwave devices with van der Waals superconductors. *arXiv* 2107.09147 (2021).
- [14] Wang, L. *et al.* One-Dimensional Electrical Contact to a Two-Dimensional Material. *Science* **342**, 614–617 (2013).
- [15] Schmidt, F. E., Jenkins, M. D., Watanabe, K., Taniguchi, T. & Steele, G. A. A ballistic graphene superconducting microwave circuit. *Nat. Comm.* **9**, 4069 (2018).
- [16] Wang, J. I.-J. *et al.* Coherent control of a hybrid superconducting circuit made with graphene-based van der Waals heterostructures. *Nat. Nanotechnol.* **14**, 120–125 (2019).
- [17] Seifert, P. *et al.* Magic-Angle Bilayer Graphene Nanocalorimeters: Toward Broadband, Energy-Resolving Single Photon Detection. *Nano Lett.* **20**, 3459 (2020).
- [18] Lee, G.-H. *et al.* Graphene-based Josephson junction microwave bolometer. *Nature* **586**, 42–46 (2020).
- [19] Kokkonemi, R. *et al.* Bolometer operating at the threshold for circuit quantum electrodynamics. *Nature* **586**, 47–51 (2020).
- [20] Liu, X. & Hersam, M. C. 2D materials for quantum information science. *Nat. Rev. Mater.* **4**, 669–684 (2019).
- [21] Blais, A., Grimsmo, A. L., Girvin, S. M. & Wallraff, A. Circuit quantum electrodynamics. *Rev. Mod. Phys.* **93**, 025005 (2021).
- [22] Patel, U. *et al.* Coherent Josephson phase qubit with a single crystal silicon capacitor. *Appl. Phys. Lett.* **102**, 012602 (2013).
- [23] Sandberg, M. *et al.* Radiation-suppressed superconduct-

ing quantum bit in a planar geometry. *Appl. Phys. Lett.* **102**, 072601 (2013).

[24] Zhao, R. *et al.* Merged-Element Transmon. *Phys. Rev. Appl.* **14**, 064006 (2020).

[25] Island, J. O., Steele, G. A., van der Zant, H. S. J. & Castellanos-Gomez, A. Thickness dependent interlayer transport in vertical MoS₂ Josephson junctions. *2D Materials* **3**, 031002 (2016).

[26] Dvir, T. *et al.* Spectroscopy of bulk and few-layer superconducting NbSe₂ with van der Waals tunnel junctions. *Nat. Comm.* **9**, 1–6 (2018).

[27] Brink, M., Chow, J. M., Hertzberg, J., Magesan, E. & Rosenblatt, S. Device challenges for near term superconducting quantum processors: frequency collisionsDevice challenges for near term superconducting quantum processors: frequency collisions. *IEEE International Electron Devices Meeting IEDM* 6.1.1 (2018).

[28] Wang, J. I. J. *et al.* Hexagonal Boron Nitride (hBN) as a Low-loss Dielectric for Superconducting Quantum Circuits and Qubits. *arXiv* 2109.00015 (2021).